Supporting Information For

Ultrathin covalent and cuprophilic interaction-assembled copper-sulfur monolayer in organic metal chalcogenide for oriented photoconductivity

Guang-Ning Liu,[*,a] Rang-Dong Xu,[a] Ming-Kun Li,[a] Yiqiang Sun,[a] Meng-Jie Zhou,[a] Rui-Yun Cai,[a] Zuo-Jiang You,[a] Xiao-Ming Jiang,[b] and Cuncheng Li[a]

[a]*School of Chemistry and Chemical Engineering, University of Jinan, Jinan Shandong 250022, PR China*

[b]*State Key Laboratory of Structural Chemistry, Fujian Institute of Research on the Structure of Matter, Chinese Academy of Sciences, Fuzhou, Fujian 350002, PR China*

Contents

S1. Experimental Section

S1.1 Materials and characterization

All reagents were purchased commercially and used without further purification. CuI, KI, 5-chloropyridine-2-thiol were provided by Macklin. Hydroiodic acid (45%) was purchased from Shanghai Kefeng Chemical Regent Co., Ltd. Ethanol and acetonitrile were purchased from Sinopharm Chemical Regent Co. Elemental analyses of C, H, and N were performed on an Elementar Vario EL III microanalyzer. Powder X-ray diffraction (PXRD) patterns were recorded on Rigaku SmartlabSE diffractometer using Cu $K\alpha$ radiation. A Perkin-Elmer Diamond thermogravimetric analyzer was used to obtain thermogravimetric analyses (TGA) curves in N_2 with a flow rate of 20 mL·min^{-1} and a ramp rate of 10 °C·min^{-1} in the temperature range 40–800 °C. An empty Al_2O_3 crucible was used as the reference. The FT-IR spectra were obtained on a Perkin-Elmer spectrophotometer using KBr disk in the range 4000–450 cm^{-1}. Optical diffuse reflectance spectra were measured at room temperature with a Shimadzu UV-3600 Plus UV-vis spectrophotometer. The instrument was equipped with an integrating sphere and controlled with a personal computer. The samples were ground into fine powder and pressed onto a thin glass slide holder. A $BaSO_4$ plate was used as a standard (100% reflectance). The absorption spectra were calculated from reflectance spectrum using the Kubelka-Munk function:[1] $\alpha/S = (1-R)^2/2R$ where α is the absorption coefficient, S is the scattering coefficient, and R is the reflectance. The Bravais-Friedel-Donnay-Harker (BFDH) morphology calculation was conducted in Mercury software 2020 3.0. The Mott-Schottky plot was measured in a three-electrode system at a frequency of 1000 Hz with a 0.5 M potassium chloride aqueous solution. The X-ray photoelectron spectroscopy was measured on a Shimadzu Kratos photoelectron spectrometer. The energy-dispersive spectroscopy mapping analysis was made on JEOL JEM-2100F machine. The atomic force microscope (AFM) measurement was performed on Bruker Dimension Icon machine. The transmission electron microscopy (TEM) images were recorded on a JEM-1400 machine. The scanning electron microscopy (SEM) images were recorded on a TESCAN MIRA4 microscope. The gold was coated on the films to get clear images. The temperature-dependent solid-state photoluminescence (TDPL) spectra were recorded on an Edinberg FLS920 fluorescence

spectrophotometer. The integrated emission intensity was fitted using equation (1), in which I_0 is the intensity at 0 K, E_b the binding energy, and k_B the Boltzmann constant.[2]

$$I(T) = \frac{I_0}{1 + Ae^{-E_b/k_B T}} \quad (1)$$

S1.2 Computational details

The X-ray crystallographic data of $[Cu(CMP)]_n$ was used to calculate its electronic structure. The calculations of density of states (DOS) were carried out using density functional theory (DFT) with one of the three nonlocal gradient-corrected exchange-correlation functionals (GGA-PBE) and performed with the CASTEP code,[3] which uses a plane wave basis set for the valence electrons and norm-conserving pseudopotential for the core electrons.[4] Pseudo-atomic calculations were performed for Cu $3d^{10}4s^1$, Cl $3s^23p^5$, S $3s^23p^4$, C $2s^22p^2$, N $2s^22p^3$ and H $1s^1$. The parameters used in the calculations and convergence criteria were set by the default values of the CASTEP code.[3]

S1.3 Photoelectrochemical measurement

The photoelectrochemical test was performed using an Au interdigital electrode. Five mg single crystals of $[Cu(CMP)]_n$ were first grounded in an agate mortar carefully, and then dispersed into 200-μL absolute ethanol to form a suspension, which were further ball milled for 30 min. After that, 3.5 μL of the well-dispersed suspension was drop-casted onto a carefully-cleaned Au electrode with a coating area of ~10 × 5 mm^2 to form a uniform thin-film. Finally, the film-electrode was dried at 40 °C under a vacuum environment. The film device of micro-$[Cu(CMP)]_n$ was fabricated the same as that of $[Cu(CMP)]_n$. For the photocurrent measurements, a 500 W Xe lamp with tunable optical power was chosen as the light source. Different band-pass filter in the range of 365–700 nm were used to get corresponding monochromatic light. All the incident intensity was adjusted with the help of a commercial optical power meter and all the electrical results were recorded by a Solartron ModuLab XM electrochemical system.

S1.4 Synthesis of $[Cu(CMP)]_n$

The single crystals of $[Cu(CMP)]_n$ were prepared by solvothermal method. Typically,

0.20 mmol CuI (0.038 g), 1.5 mmol KI (0.249 g) and 0.25 mmol 5-chloro-2-mercaptopyridine (CMP, 0.037 g) were dispersed in 3 mL H_2O, 3 mL acetonitrile and 1 mL HI (45%). Then, the mixture was heated to 140 °C for 3 days. Orange plate crystals were in the submillimeter scale and were got with 48% yield (based on Cu).

S1.5 Synthesis of micro-[Cu(CMP)]$_n$

The single crystals with size in the micrometer scale can be obtained via a surfactant-mediated synthesis. Typically, 0.20 mmol CuI (0.038 g), 0.25 mmol CMP (0.037 g) and 0.07 mmol cetyltrimethyl ammonium bromide (CTAB, 0.024 g) were added in a mixed solvent of 3 mL H_2O and 3 mL acetonitrile. The suspension was ultrasonic treated for 30 minutes and transferred into a 25-mL poly(tetrafluoroethylene)-lined stainless steel container under autogenous pressure and then heated at 140 °C for 6 hours and finally cooled to room temperature. The product were filtered and washed with water, ethanol and acetonitrile successively. Regular sheet-like single crystals were isolated as the pure phase. The shape and size of the single crystals were determined by an optical microscope.

S 2 Single-crystal structure determination

The intensity data sets were collected on a Agilent Xcalibur, Eos, Gemini CCD diffractometer equipped with a graphite-monochromated Mo Kα radiation (λ = 0.71073 Å) at 293 K. The data sets were reduced by the CrysAlisPro[5] program. An empirical absorption correction using spherical harmonics was implemented in SCALE3 ABSPACK scaling algorithm. The structures were solved by direct methods using the Siemens SHELXL package of crystallographic software.[6] Difference Fourier maps were created on the basis of these atomic positions to yield the other non-hydrogen atoms. The structures were refined using a full-matrix least-squares refinement on F^2. All non-hydrogen atoms were refined anisotropically. The hydrogen atoms were located at geometrically calculated positions and refined as riding on their parent atoms with fixed isotropic displacement parameters [U_{iso}(H) = 1.2U_{eq}(C, N)]. Crystallographic data and structural refinements for four hybrids are summarized in Table S1. Important bond lengths and angles are listed in Table S5.

Table S1. Crystallographic Data.

Formula	$C_5H_3NSClCu$
M_r (g mol^{-1})	208.13
Crystal system	Monoclinic
Space group	$P2_1/c$
ρ_{calcd} [g cm^{-3}]	2.304
a [Å]	13.6065(5)
b [Å]	5.9981(3)
c [Å]	7.4480(3)
α [°]	90
β [°]	99.156(4)
γ [°]	90
V [Å^3]	600.11(4)
Z	4
F (000)	408.0
θ range [°]	6.066–58.346
Measured reflections	5660
Independent reflections (R_{int})	1468 (R_{int} = 0.0353)
Data/params/restraints	2468/0/82/
R_1[a], wR_2[b] [I>2s(I)]	0.0325, 0.0721
Goodness of fit	1.047
$\Delta\rho_{max}$ and $\Delta\rho_{min}$ [e Å^{-3}]	0.62, –0.37

[a]$R_1 = \sum||F_o|-|F_c||/\sum|F_o|$, [b]w$R_2 = \{\sum w[(F_o)^2-(F_c)^2]^2/\sum w[(F_o)^2]^2\}^{1/2}$

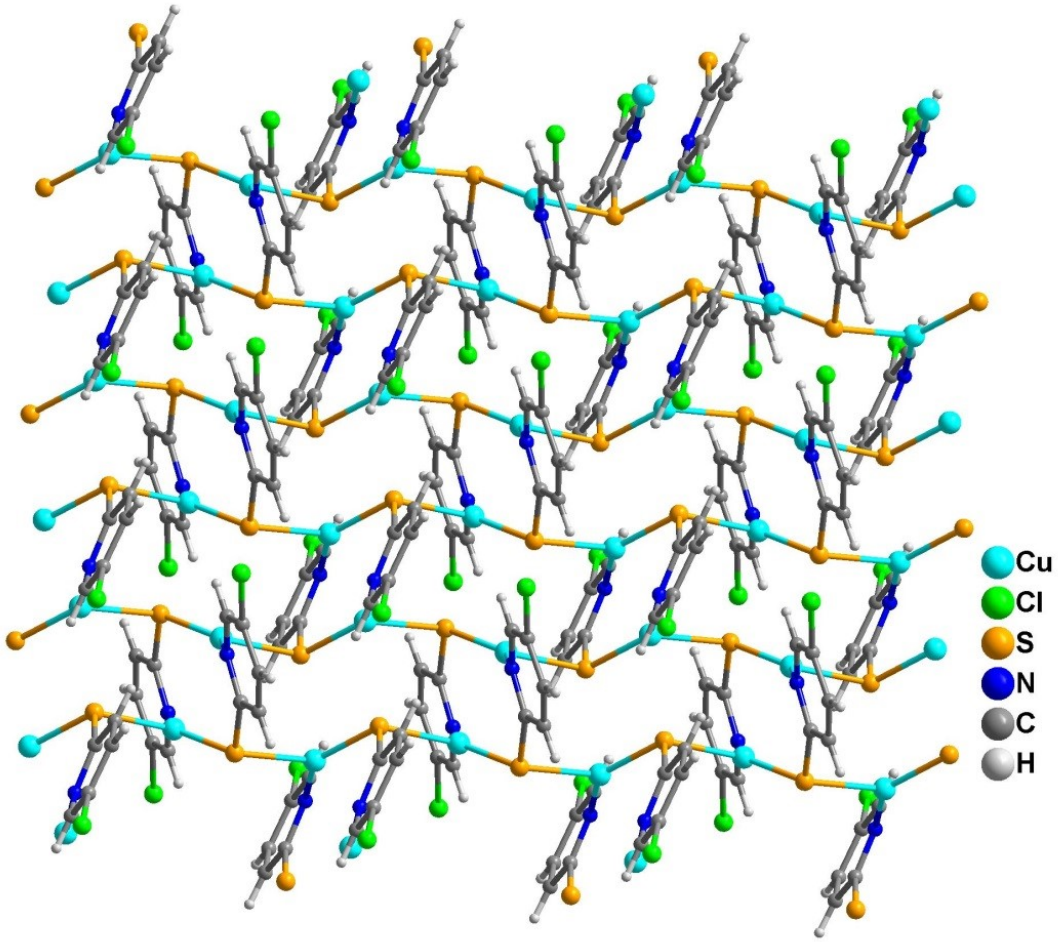

Fig. S1 The 2D hybrid layer of $[Cu(CMP)]_n$.

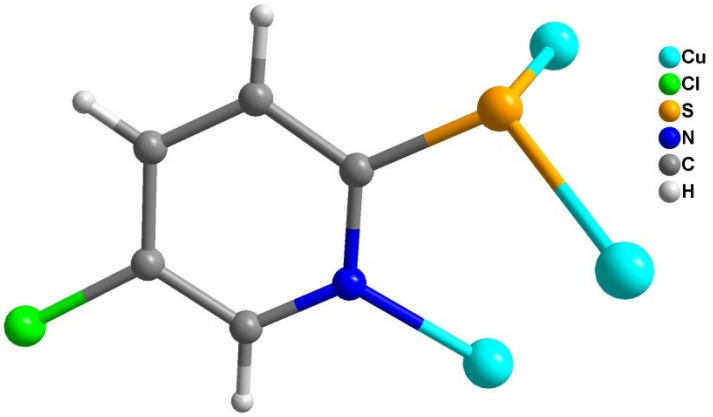

Fig. S2 Presentation of the coordination mode of the CMP ligand.

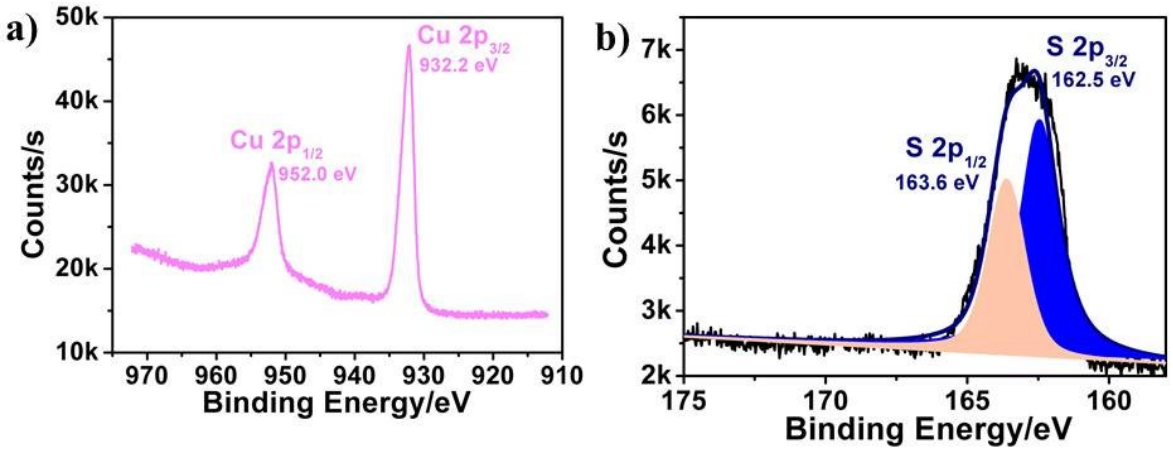

Fig. S3 XPS spectra for $[Cu(CMP)]_n$; (a) Cu 2p region and (b) S 2p region for $[Cu(CMP)]_n$.

The two intense peaks at 932.2 eV and 952.0 in the Cu 2p spectrum are ascribed to the Cu $2p_{3/2}$ and Cu $2p_{1/2}$, respectively. The absence of the satellite signal of Cu (II) between the two peaks firmly indicate that the valence of Cu in $[Cu(CMP)]_n$ is mono-valence. The S $2p_{3/2}$ peak in the S 2p XPS spectrum locates at 162.5 eV is ascribed to the S atoms from CMP ligand coordinating to Cu.[7]

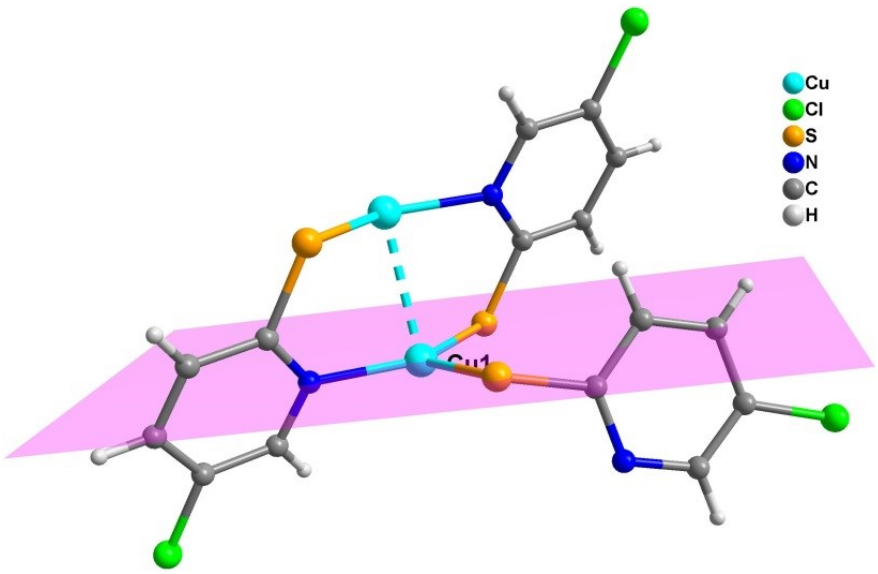

Fig. S4 Presentation of the coordination sphere of Cu atom in $[Cu(CMP)]_n$, where each Cu atom is coordinated by two sulfydryl S atom and one pyridine N atoms from three CMP ligands.

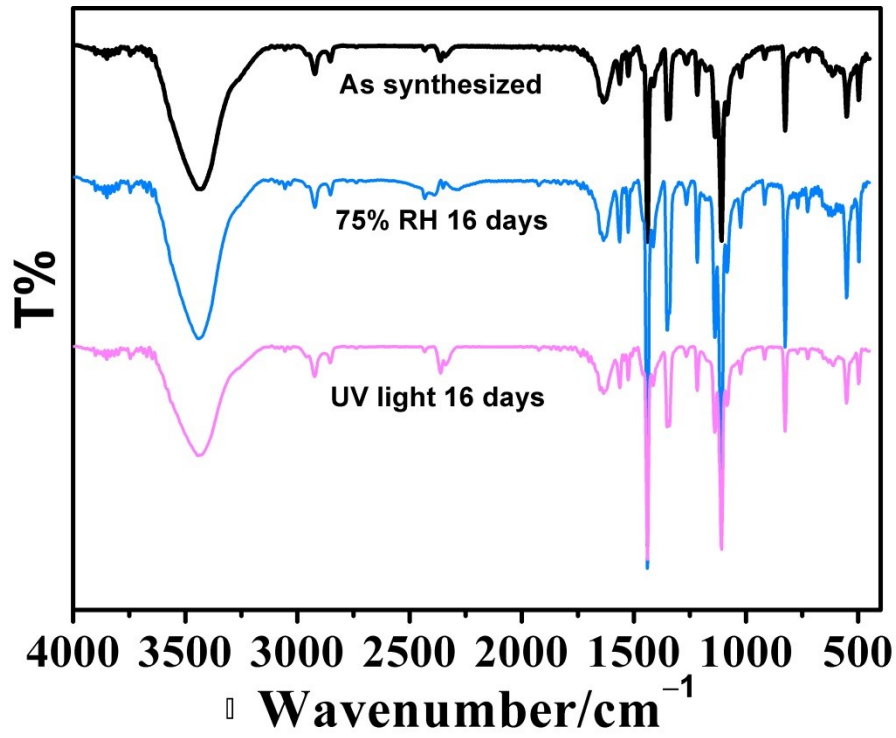

Fig. S5 IR spectra of $[Cu(CMP)]_n$ under different conditions.

Table S2. IR Spectral Data (KBr pellet, cm^{-1}).

Compound	Peak position
$[Cu(CMP)]_n$	3434(m), 3051(w), 2923(w), 2430(vw), 1633(vw), 1559(m), 1436(vs), 1344(s), 1261(w), 1217(m), 1140(m), 1106(vs), 1018(m), 915(w), 825(s), 767(vw), 726(vw), 647(vw), 655 (vw), 550(s).

IR analysis: The weak peak at 3051 cm^{-1} is ascribed to the C–H vibrations of the aromatic ring hydrogen atoms, ν(=C-H). The bands in the range 1640–1400 cm^{-1} are assigned to the bands of ring vibrations of the conjugated ligand (ν(C=C) and ν(C=N)). The bands of the Ar–S stretching vibration appear at 1018 cm^{-1} and 647 cm^{-1}. The strong peak at 825 cm^{-1} could be ascribed to the C–Cl vibrations of the CMP molecule. All these demonstrate the introduction of CMP in the 2D material. The broad band at 3434 cm^{-1} is assigned to the stretching of trace water since the measurements were conducted in air. These results agree with the SXRD studies.

Table S3. The C, H, and N Elemental Analysis.

$[Cu(CMP)]_n$	C	H	N
Theoretical	28.85	1.45	6.73
Experimental	28.58	1.42	6.91

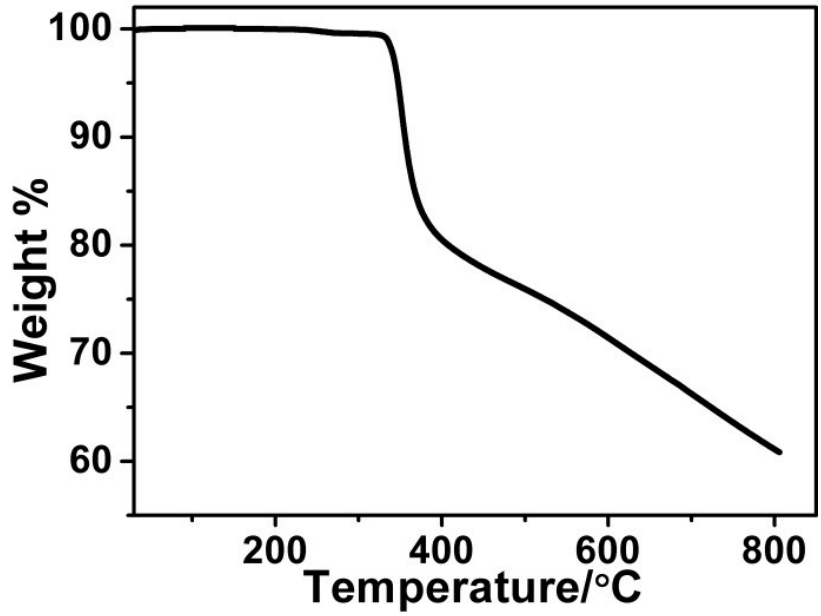

Fig. S6 The TGA curve for $[Cu(CMP)]_n$.

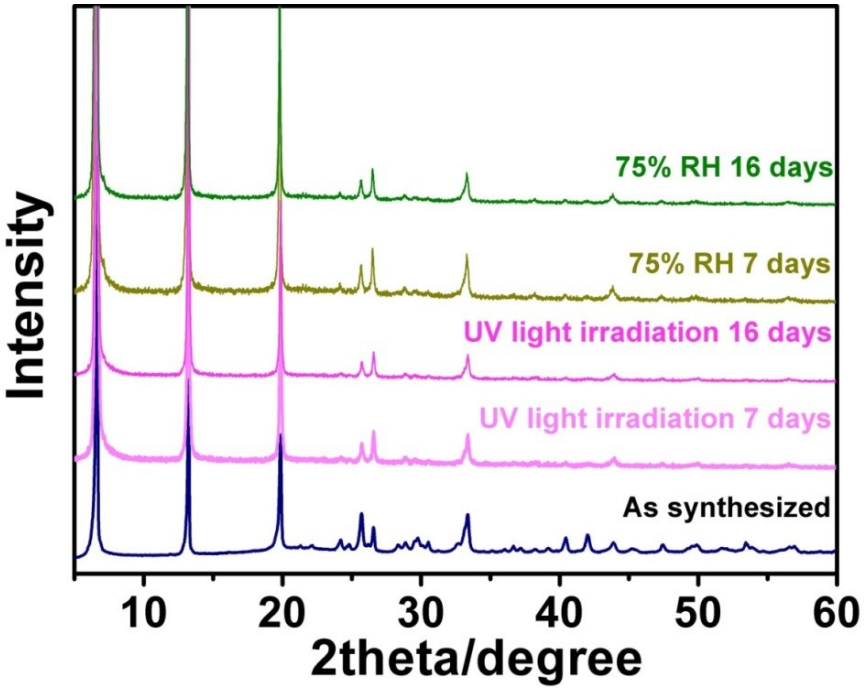

Fig. S7 The PXRD patterns for $[Cu(CMP)]_n$ after moisture and light stability experiments.

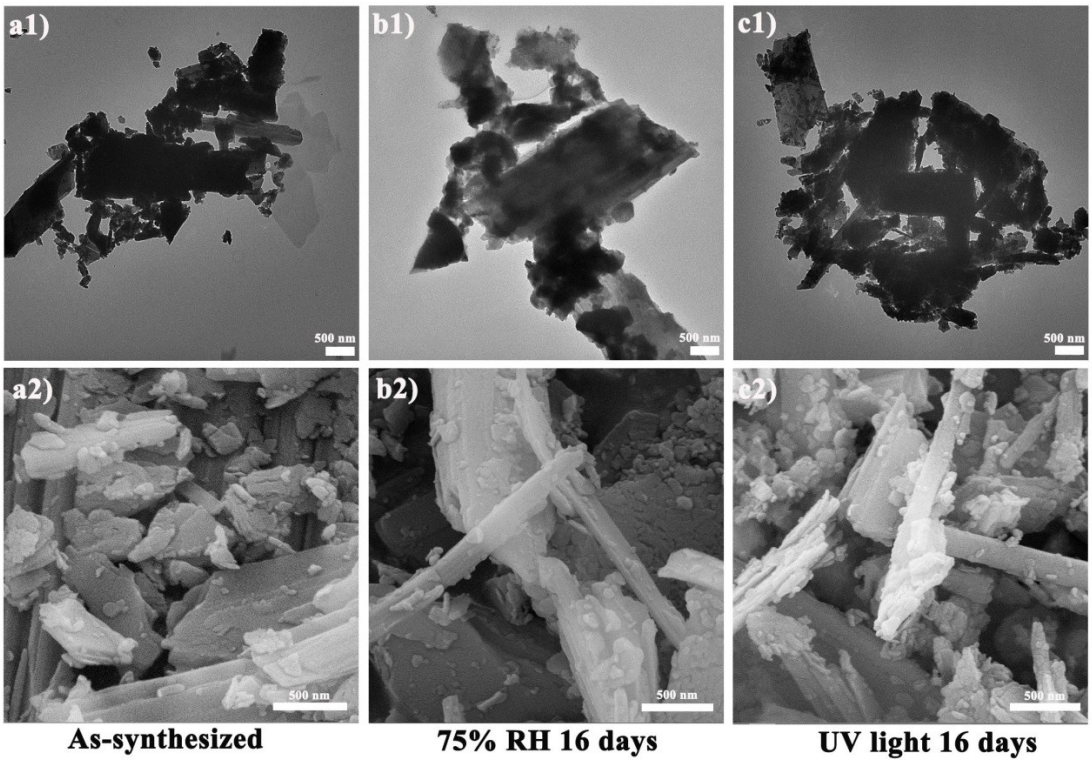

Fig. S8 The TEM and SEM images of the as-synthesized polycrystalline powder of $[Cu(CMP)]_n$ (a1 and a2), the powder after 75% RH treatment for 16 days (b1 and b2), and the powder after UV light irradiation for 16 days (c1 and c2), respectively.

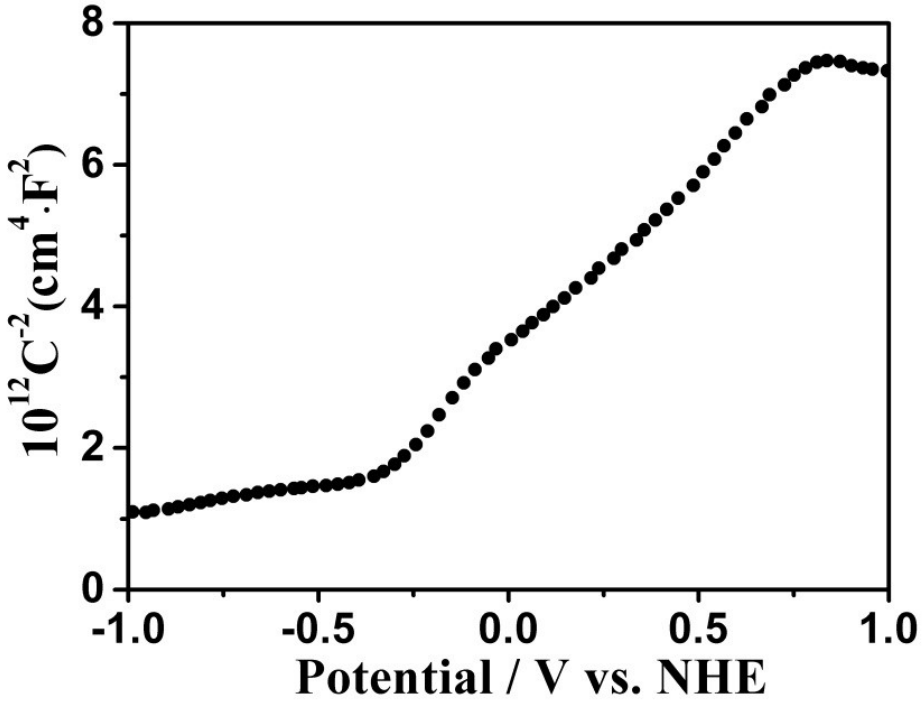

Fig. S9 The Mott-Schottky plot of $[Cu(CMP)]_n$.

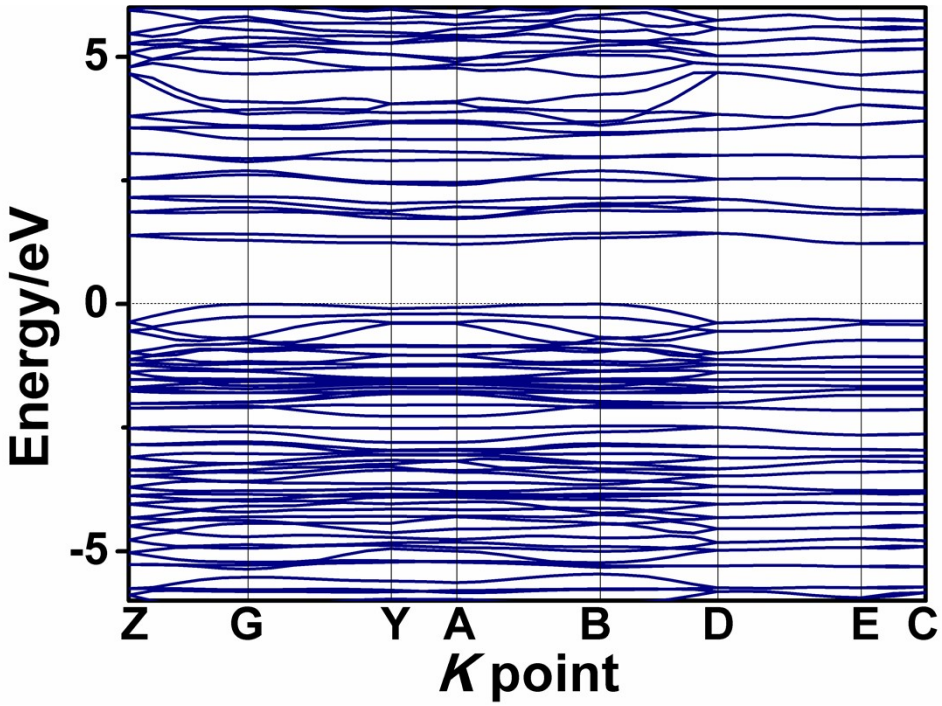

Fig. S10 The band structure of $[Cu(CMP)]_n$ showing the indirect band gap feature.

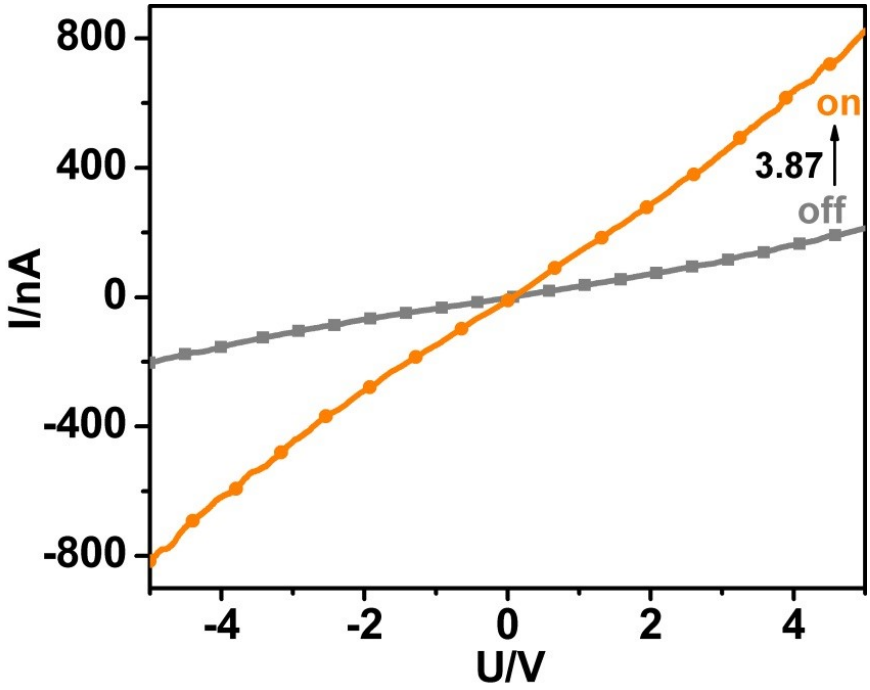

Fig. S11 The I−V curves of the $MA_3Bi_2I_9$ film device in the dark and under white light irradiation (85 mW·cm^{-2}). The fabrication and measurement of the device are under the same conditions as those for $[Cu(CMP)]_n$ device.

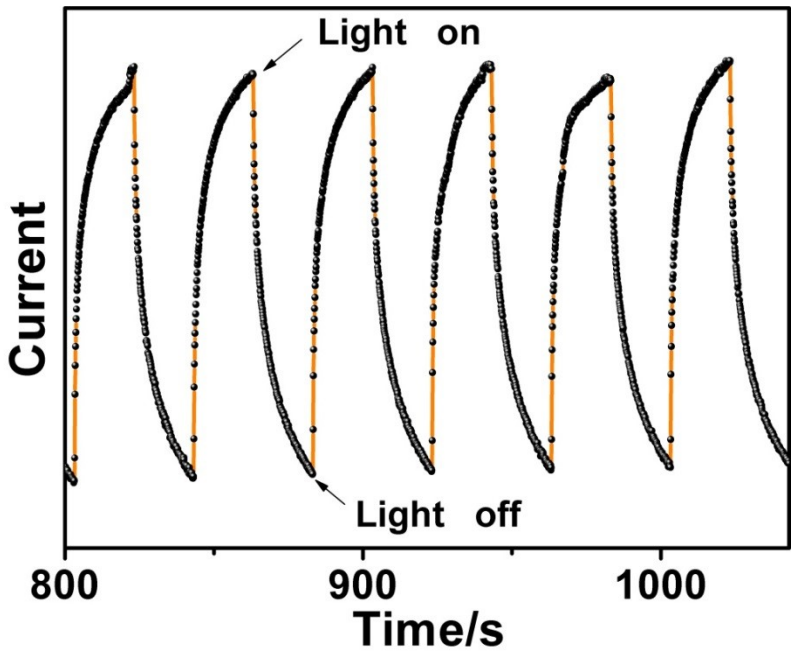

Fig. S12 Dynamic I-T curve when a positive bias voltage of 2 V was applied for the $[Cu(CMP)]_n$ film device fabricated by milled method.

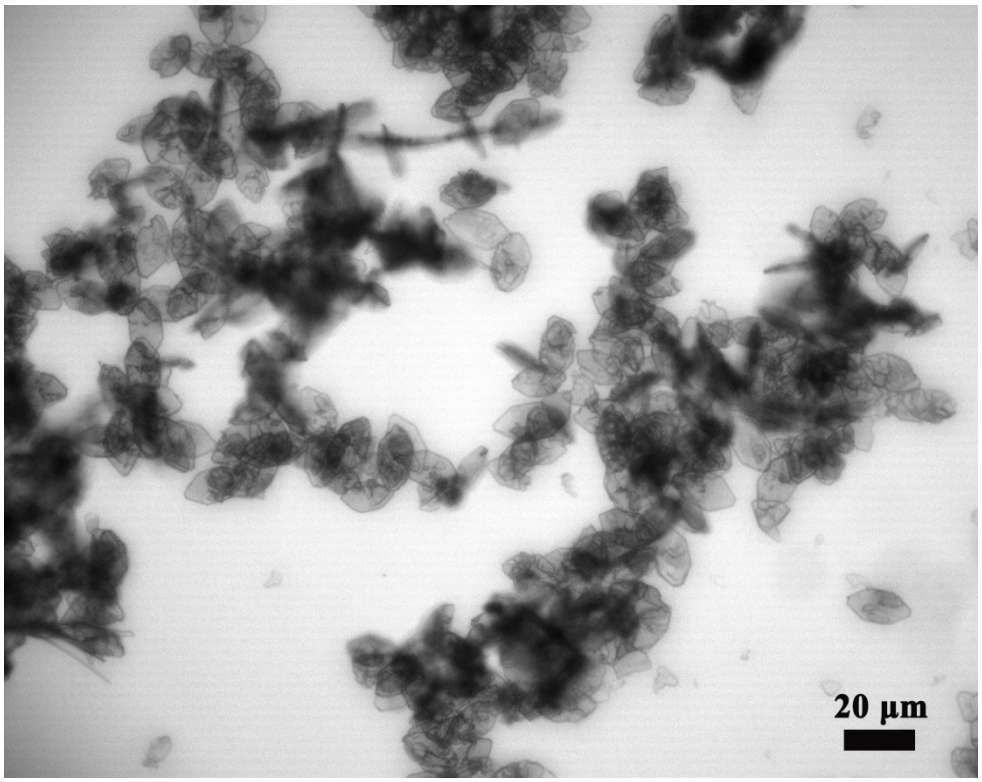

Fig. S13 Photograph of micro-$[Cu(CMP)]_n$ crystals.

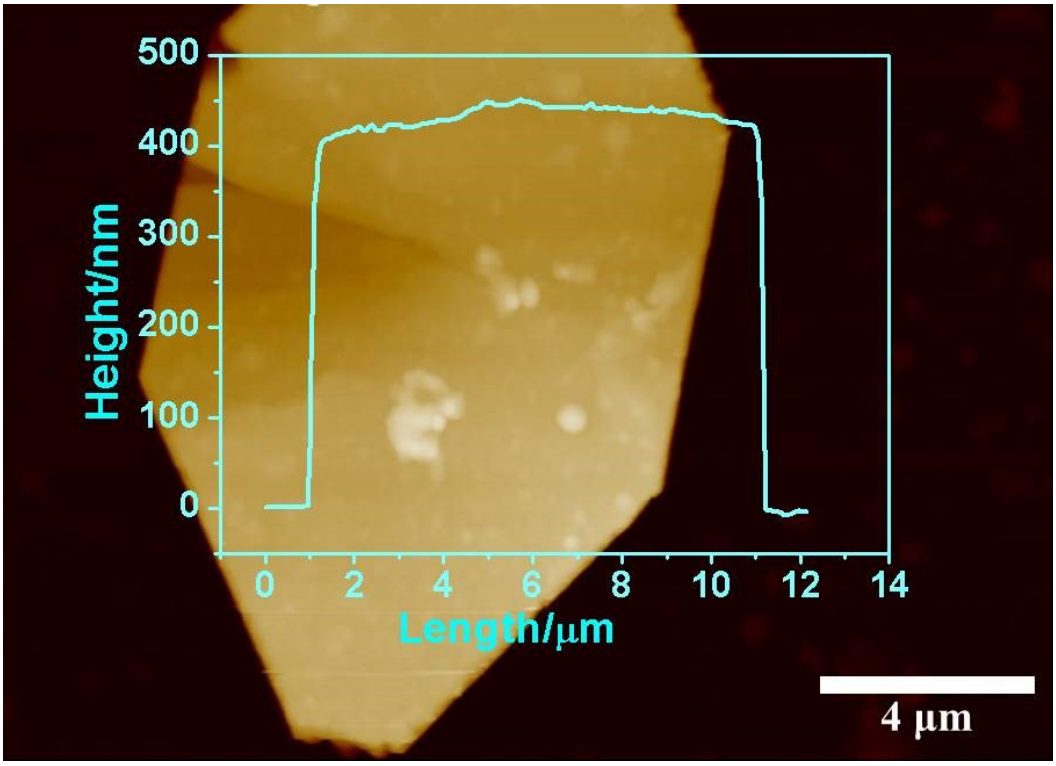

Fig. S14 The AFM image of a micro-[Cu(CMP)]$_n$ crystal.

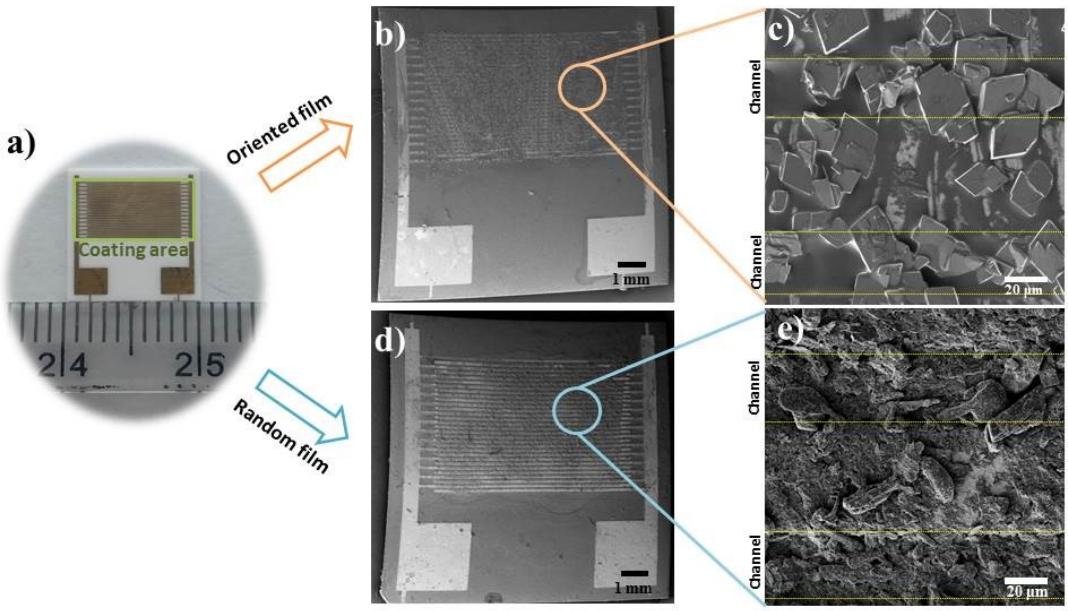

Fig. S15 (a) The optical photograph of a blank interdigital electrode showing the coating area of the film. (b, c) The SEM images of the oriented film of the micro-[Cu(CMP)]$_n$ sheet-like crystals. (d, e) The SEM images of the random film of the grinded [Cu(CMP)]$_n$ crystals. The channel of the interdigital electrode are marked by yellow dashed lines in panels c and e.

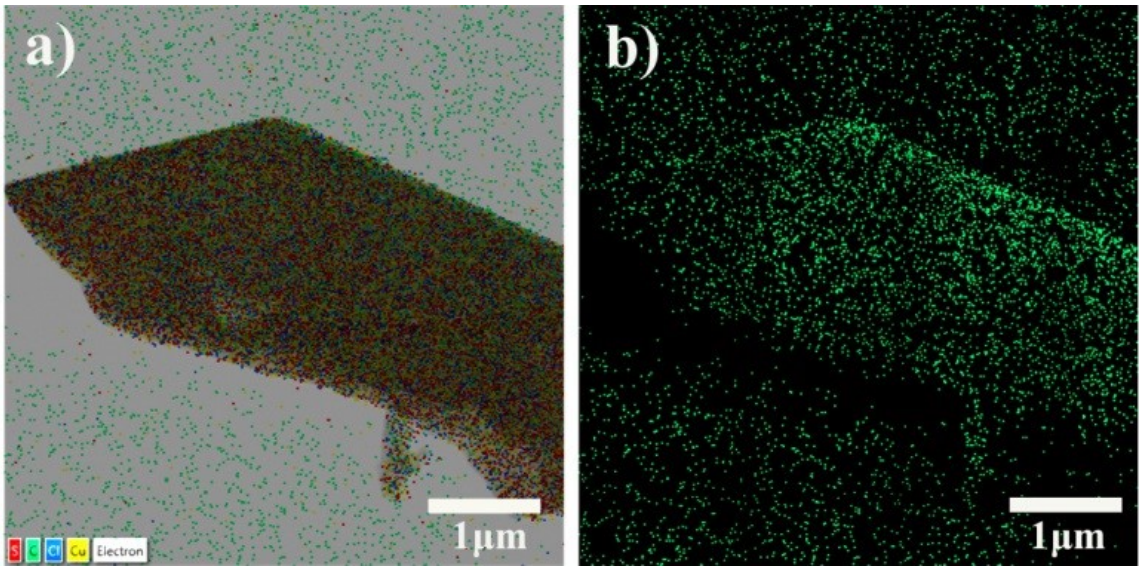

Fig. S16 (a) The EDS layered image. (b) The C element mapping analysis.

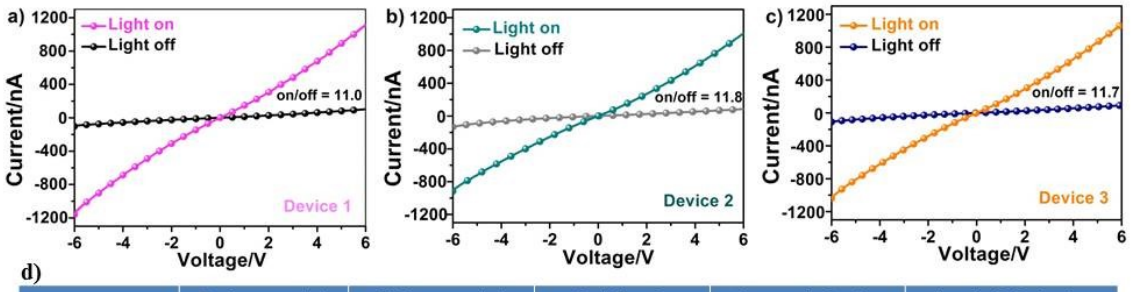

d)

	Dark current/nA	Light current/nA	On/off ratio	Average derivation	Standard derivation
Device 1	81.2	892	11.0		
Device 2	68.1	804	11.8	0.33	0.44
Device 3	73.7	861	11.7		

Fig. S17 (a–c) The I−V curves of three micro-$[Cu(CMP)]_n$ film devices in the dark and under white light irradiation (85 $mW \cdot cm^{-2}$). The devices have comparable conductivities and photoresponses, implying the good reproducibility of the electrical measurements. (d) The average and standard deviations of the three devices. The dark and light currents under the bias of 5 V were employed to get the on/off ratios of the devices.

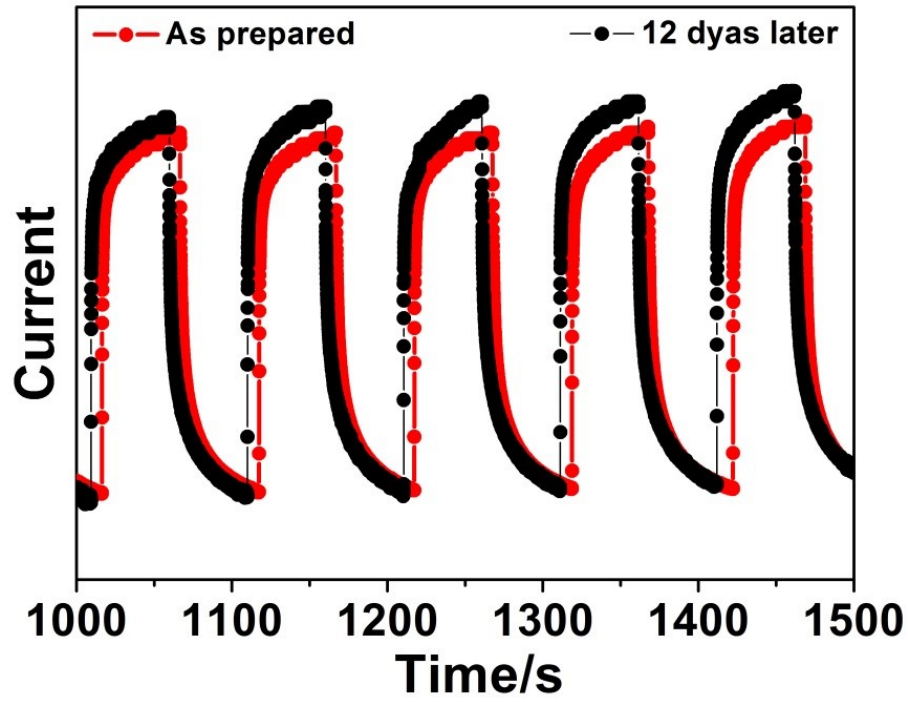

Fig. S18 Dynamic I-T curves of the micro-$[Cu(CMP)]_n$ film device after stored in the laboratory for 12 days.

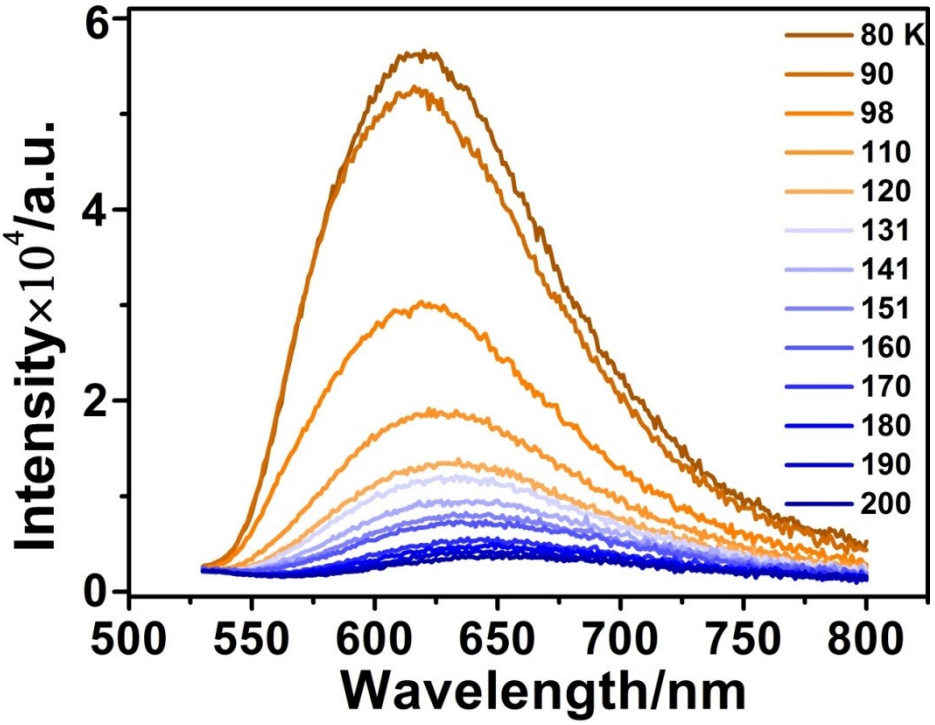

Fig. S19 The TDPL photoluminescence emission spectra of $[Cu(CMP)]_n$ in the temperature range of 80–200 K.

Table S4. Summary of the Photodetection Device Parameters.

Material	Device type	Resistance (Ω)	Response range (nm)	On/off ratio	Eg (eV)	Reference
micro-$[Cu(CMP)]_n$	Thin film	5.9×10^7	400-700	11.0	2.44	This work
$K_2Cu_2Cl_6$	Thin film	NA	330-390	1.9	1.85	8
$CsCuCl_3$	Thin film	2.9×10^4	369	30	1.92	9
$CuBiI_4$	Thin film	NA	532	2.2	1.84	10
$Cs_3Cu_2I_5$	Thin film	1×10^6	265/365	127	3.8	11
$[Cu_6I_3(TP)_3(MeCN)_2]_n$	NA	8.3×10^5	NA	NA	1.98	12
$(Mebtz)_2Cu_3I_5$	Thin film	2.92×10^3	white light	35.4	2.4	13

TP = Thiophenol; MeCN = Acetonitrile; Mebtz = Methylbenzothiazole.

Table S5. Selected Bond Distances (Å) and Angles (°) for $[Cu(CMP)]_n$.

$[Cu(CMP)]_n$			
Bond	(Å)	Bond	(Å)
Cu(1)-Cu(1)#1	2.6766(8)	S(1)-C(5)	1.758(3)
Cu(1)-S(1)#1	2.2355(8)	N(1)-C(1)	1.345(4)
Cu(1)-S(1)#2	2.3226(8)	N(1)-C(5)	1.350(4)
Cu(1)-N(1)	1.999(2)	C(1)-C(2)	1.376(4)
Cl(1)-C(2)	1.736(3)	C(2)-C(3)	1.389(5)
S(1)-Cu(1)#3	2.3226(8)	C(3)-C(4)	1.370(4)
S(1)-Cu(1)#1	2.2355(8)	C(4)-C(5)	1.401(4)
Angle	(°)	Angle	(°)
S(1)#1-Cu(1)-Cu(1)#1	81.74(2)	C(5)-N(1)-Cu(1)	119.46(18)
S(1)#2-Cu(1)-Cu(1)#1	101.92(3)	N(1)-C(1)-C(2)	122.4(3)
S(1)#1-Cu(1)-S(1)#2	114.27(3)	C(1)-C(2)-Cl(1)	119.5(2)
N(1)-Cu(1)-Cu(1)#1	86.70(7)	C(1)-C(2)-C(3)	119.6(3)
N(1)-Cu(1)-S(1)#2	107.81(7)	C(3)-C(2)-Cl(1)	120.8(2)
N(1)-Cu(1)-S(1)#1	137.79(7)	C(4)-C(3)-C(2)	118.0(3)
Cu(1)#1-S(1)-Cu(1)#3	112.04(3)	C(3)-C(4)-C(5)	120.4(3)
C(5)-S(1)-Cu(1)#3	105.75(10)	N(1)-C(5)-S(1)	118.9(2)
C(5)-S(1)-Cu(1)#1	105.87(10)	N(1)-C(5)-C(4)	120.7(3)
C(1)-N(1)-Cu(1)	120.66(19)	C(4)-C(5)-S(1)	120.4(2)
C(1)-N(1)-C(5)	118.7(2)		

Symmetry transformations used to generate equivalent atoms: #1 -x+1, -y+1, -z+1; #2 -x+1, y-1/2, -z+3/2; #3 -x+1, y+1/2, -z+3/2.

Reference

1. W. M. Wendlandt, H. G. Hecht, *Reflectance Spectroscopy*. Interscience: New York, 1966.
2. K. Wu, A. Bera, C. Ma, Y. Du, Y. Yang, L. Li, T. Wu, *Phys. Chem. Chem. Phys.,* 2014, **16**, 22476-22481.
3. (a) M. D. Segall, P. J. D. Lindan, M. J. Probert, C. J. Pickard, P. J. Hasnip, S. J. Clark, M. C. Payne, *J. Phys.: Condens. Matter,* 2002**, 14**, 2717-2744; (b) V. Milman, B. Winkler, J. A. White, C. J. Pickard, M. C. Payne, E. V. Akhmatskaya, R. H. Nobes, *Int. J. Quantum Chem.,* 2000, **77**, 895-910.
4. D. R. Hamann, M. Schluter, C. Chiang, *Phys. Rev. Lett.,* 1979, **43**, 1494-1497.
5. Agilent, *CrysAlisPro*. Version 1.171.35.21 ed.; Agilent Technologies Corp.: California, America.
6. Siemens, *SHELXTL Version 5 Reference manual*. Siemens Energy & Automaion Inc.: Madision,WI, 1994.
7. (a) P. E. Laibinis, G. M. Whitesides, *J.am.chem.soc,* 1992**, 144**, 9022-9028; (b) Y. Joseph, I. Besnard, M. Rosenberger, B. Guse, T. Vossmeyer, *J. Phys. Chem. B,* 2003, **107**, 7406-7413; (c) H. Ning, Y. Zeng, S. Zuo, S. V. Kershaw, Y. Hou, Y. Li, X. Li, J. Zhang, Y. Yi, L. Jing, J. Li, M. Gao, *ACS Nano,* 2021, **15**, 873-883.
8. H. Zhou, X. Liu, G. He, L. Fan, S. Shi, J. Wei, W. Xu, C. Yuan, N. Chai, B. Chen, Y. Zhang, X. Zhang, J. Zhao, X. Wei, J. Yin, D. Tain, *ACS Omega,* 2018, **3**, 14021-14026.
9. S. Cui, Y. Chen, S. Tao, J. Cui, C. Yuan, N. Yu, H. Zhou, J. Yin, X. Zhang, *Eur. J. Inorg. Chem.,* 2020, **2020**, 2165-2169.
10. N. Qu, Y. Lei, X. Yang, X. Hu, W. Zhao, C. Zhao, Z. Zheng, *J. Mater. Chem. C,* 2020, **8**, 8451-8456.
11. Z.-X. Zhang, C. Li, Y. Lu, X.-W. Tong, F.-X. Liang, X.-Y. Zhao, D. Wu, C. Xie, L.-B. Luo, *J. Phys. Chem. Lett.,* 2019**, 10**, 5343-5350.
12. Y. Sun, M. Amsler, S. Goedecker, A. Caravella, M. Yoshida, M. Kato, *Crystengcomm,* 2019, **21**, 3948-3953.
13. R.-Y. Zhao, G.-N. Liu, Q.-S. Liu, P.-F. Niu, R.-D. Xu, Z.-H. Wang, T.-H. Wei, J. Zhang, Y.-Q. Sun, C.. Li, *Crys. Grow. & Des.,* 2020, **20**, 1009-1015.